Effect of biofilm structural deformation on hydraulic resistance during ultrafiltration
A numerical and experimental study

Jafari, Morez; Desmond, Peter; van Loosdrecht, Mark C.M.; Derlon, Nicolas; Morgenroth, Eberhard; Picioreanu, Cristian

DOI
10.1016/j.watres.2018.08.036

Publication date
2018

Document Version
Final published version

Published in
Water Research

Citation (APA)
Jafari, M., Desmond, P., van Loosdrecht, M. C. M., Derlon, N., Morgenroth, E., & Picioreanu, C. (2018). Effect of biofilm structural deformation on hydraulic resistance during ultrafiltration: A numerical and experimental study. *Water Research*, *145*, 375-387. https://doi.org/10.1016/j.watres.2018.08.036

Water Research 145 (2018) 375–387

Contents lists available at ScienceDirect

Water Research

journal homepage: www.elsevier.com/locate/watres

Effect of biofilm structural deformation on hydraulic resistance during ultrafiltration: A numerical and experimental study

Morez Jafari [a, *], Peter Desmond [b, c], Mark C.M. van Loosdrecht [a], Nicolas Derlon [b], Eberhard Morgenroth [b, c], Cristian Picioreanu [a]

[a] Department of Biotechnology, Faculty of Applied Sciences, Delft University of Technology, Van der Maasweg 9, 2629, HZ, Delft, The Netherlands
[b] Eawag, Swiss Federal Institute of Aquatic Science and Technology, 8600, Dübendorf, Switzerland
[c] ETH Zürich, Institute of Environmental Engineering, 8093, Zürich, Switzerland

ARTICLE INFO

Article history:
Received 23 May 2018
Received in revised form
14 August 2018
Accepted 18 August 2018
Available online 18 August 2018

Keywords:
Biofilm compression
Hydraulic resistance
Fluid-structural model
Elastic modulus
Poroelasticity

ABSTRACT

Biofilm formation in membrane systems negatively impacts the filtration system performances. This study evaluated how biofilm compression driven by permeate flow increases the hydraulic resistance and leads to reduction in permeate flux. We analysed the effect of biofilm compression on hydraulic resistance and permeate flux through computational models supported by experimental data. Biofilms with homogeneous surface structure were subjected to step-wise changes in flux and transmembrane pressure during compression and relaxation tests. Biofilm thickness under applied forces was measured non-invasively *in-situ* using optical coherence tomography (OCT). A numerical model of poroelasticity, which couples water flow through the biofilm with biofilm mechanics, was developed to correlate the structural deformation with biofilm hydraulics (permeability and resistance). The computational model enabled extracting mechanical and hydrological parameters corresponding to the experimental data. Homogeneous biofilms under elevated compression forces experienced a significant reduction in thickness while only a slight increase in resistance was observed. This shows that hydraulic resistance of homogeneous biofilms was affected more by permeability decrease due to pore closure than by a decrease in thickness. Both viscoelastic and elastoplastic models could describe well the permanent biofilm deformation. However, for biofilms under study, a simpler elastic model could also be used due to the small irreversible deformations. The elastic moduli fitting the measured data were in agreement with other reported values for biofilm under compression. Biofilm stiffening under larger flow-driven compression forces was observed and described numerically by correlating inversely the elastic modulus with biofilm porosity. The importance of this newly developed method lies in estimation of accurate biofilm mechanical parameters to be used in numerical models for both membrane filtration system and biofouling cleaning strategies. Such model can ultimately be used to identify optimal operating conditions for membrane system subjected to biofouling.

1. Introduction

In the recent decades, membrane processes have become established technologies in drinking water and wastewater treatment. Production of stable water quantity and quality are now usual characteristics for membrane systems. However, due to the non-sterile conditions, microorganisms are present in water and formation of biofilms is inevitable, leading to biofouling (Vrouwenvelder et al., 1998), reduction of water production (Li and Elimelech, 2004) and life time reduction of membrane modules (Martin et al., 2014). Biofilms developed on membranes have a negative impact on both cross flow (i.e., increased axial pressure drop; Vrouwenvelder et al. (2009)) and on permeate flow (i.e., reduced water flux; Lee et al. (2010)). The additional hydraulic resistance induced by biofilms (Dreszer et al., 2013) reduces permeate flux in microfiltration (MF) and ultrafiltration (UF) (Martin et al., 2014). In reverse osmosis (RO) and forward osmosis (FO), where the hydraulic resistance of membrane is dominant, biofilms decrease the flux mainly by enhancing the concentration polarization (thus decreasing the

---

* Corresponding author.
E-mail address: M.Jafarieshlaghi@tudelft.nl (M. Jafari).

https://doi.org/10.1016/j.watres.2018.08.036
0043-1354/

net pressure by causing extra osmotic pressure) (Herzberg and Elimelech, 2007; Radu et al., 2010). The hydraulic resistance, in turn, depends on the biofilm thickness and permeability. On the other hand, biofilm permeability depends on biofilm porosity and tortuosity. It has been reported that water permeation through biofilms can cause a structural re-arrangement, increasing biofilm density (Casey, 2007), decreasing the porosity and eventually increasing the hydraulic resistance (Derlon et al., 2016; Dreszer et al., 2013; Valladares Linares et al., 2015). The extent of biofilm compression will be the result of a balance between forces generated by the permeate flow (i.e., pore pressure and permeate drag) and structural forces opposing biofilm deformation (i.e., elastic, viscous). At the same time, the biofilm compression caused by permeation would lead to an elevated mechanical strength, with biofilms more difficult to be removed during the cleaning. Other studies also observed biofilm hardening behaviour under elevated stress (Laspidou, 2007; Paramonova et al., 2009). Compression of organic fouling layers developed on FO and RO by permeate drag force membranes has been reported (Xie et al., 2015). Therefore, it appears important to relate the biofilm hydraulic resistance both with the applied hydrodynamic conditions and with the biofilm mechanical behaviour. A better understanding of the link between the hydrodynamic conditions, the biofilm mechanical properties and its resulting hydraulic resistance is required to properly define operating strategies for membrane processes. An optimal operation of membrane systems should aim at maximizing permeate flux while minimizing compression of the biofilms.

Recently, the biofilm compression in gravity-driven membrane filtration (GDM) has been recorded with optical coherence tomography (OCT) (Desmond et al., 2018). During dead-end ultrafiltration, the biofilm experiences only compression forces. Several studies correlated biofilm mechanical behaviour and properties (e.g., Young modulus, bulk modulus, relaxation time, etc.) to the different flow conditions: shear forces (i.e., flow parallel to biofilm surface caused by axial flow; Blauert et al. (2015)), compression forces (i.e., permeate flow perpendicular to biofilm and membrane surfaces (Derlon et al., 2016);) and simultaneous compression and shear (Valladares Linares et al., 2015)). However, there is still no theoretical description of biofilm deformation under compression forces caused by water permeation.

To improve our understanding of biofilm compression and its effect on hydraulic resistance in membrane filtration processes, we formulated a numerical model coupling the permeate flow with the biofilm mechanics. The numerical model was used to explain experimental observations of changing biofilm thickness and hydraulic resistance under compression and relaxation generated by different applied fluxes and transmembrane pressure in a dead-end ultrafiltration system. Model simulations were also used to extract mechanical and hydrological parameters corresponding to the experimental data. Finally, we evaluated the effect of different mechanical and structural properties of biofilms on the hydraulic response of biofilms to applied permeate flux.

2. Experimental set-up

2.1. Biofilm growth and compression setup

Biofilms were grown for 20 days under constant transmembrane pressure (TMP) of 0.06 bar in Membrane Fouling Simulators (MFS) according to Desmond et al. (2018). Feed waters with different compositions (i.e., river water and synthetic water with phosphorous limitation) were used for the cultivation of the biofilms on membrane surfaces. The compression/relaxation experiments were performed by step-wise increase/decrease of the permeate flux (L/m^2/h) (Fig. 1a) or TMP (bar) (Fig. 1b) to defined values. TMP controlled experiments have been carried out by monitoring pressure at the feed and permeate side, while permeate flux was controlled using permeate mass measurements and PID control.

2.2. Compression set-up and membrane preparation

Biofilms which were developed for 20 days under constant TMP of 0.06 bar in six MFS in a gravity driven membrane were subjected to a compression/relaxation scheme in an automated filtration system, as descried in details by Desmond et al. (2018). The automated filtration system was fed with feed waters reflective of the biofilm growth conditions. The filtration system mainly consisted of a gear pump, a transparent MFS (in which biofilms were already developed), measurement scales and PID control system.

Ultrafiltration membranes (UP150, MicrodyN Nadir, Wiesbaden, Germany) with molecular weight cut-off MWCO = 150 kDa and the equivalent pore size of 30–40 nm were used in MFS units. Membrane coupons were cut and rinsed with 40% ethanol prior to use in MFS.

2.3. Hydraulic parameters

The biofilm hydraulic resistance R_{bio} [1/m] was calculated as the difference between the total hydraulic resistance R_{tot} and membrane resistance R_{mem}. The total filtration resistance is a function of transmembrane pressure, TMP [Pa], water viscosity, μ [Pa•s] (at 15 °C) and the measured permeate flux J [m/s] in the presence of biofilm (Darcy's law):

$$R_{tot} = \frac{TMP}{J\,\mu} \tag{1}$$

The bare membrane resistance, R_{mem}, is the intrinsic resistance measured with nanopure water prior to fouling. The permeate flux in [L/m^2/h] was calculated from mass measurements of permeate collection, as follows:

$$J = \frac{\Delta m}{\rho_w A\, \Delta t} \tag{2}$$

with Δm the mass of collected permeate [kg], ρ_w the water density [kg/L], A the membrane active area [m^2] and Δt the permeate collection time [h].

2.4. Biofilm morphology quantification

The morphological response of the membrane biofilms to increasing and decreasing compressive force was measured by means of optical coherence tomography (OCT) (model 930 nm Spectral Domain, Thorlabs GmbH, Dachau, Germany) with a central light source wavelength of 930 nm and refractive index of 1.33 (Desmond et al., 2018). Quantification of average biofilm thickness and surface roughness were conducted using a customized MATLAB routine (MathWorks, Natick, US).

3. Model description

A mathematical model was developed to evaluate the effects of biofilm deformation (compression and relaxation) on the biofilm hydraulic resistance under step-wise flux or TMP in dead-end ultrafiltration. The model couples fluid flow in the biofilm considered as porous medium with the structural mechanics of biofilm. The liquid pressure in biofilm pores affects the effective stress in the

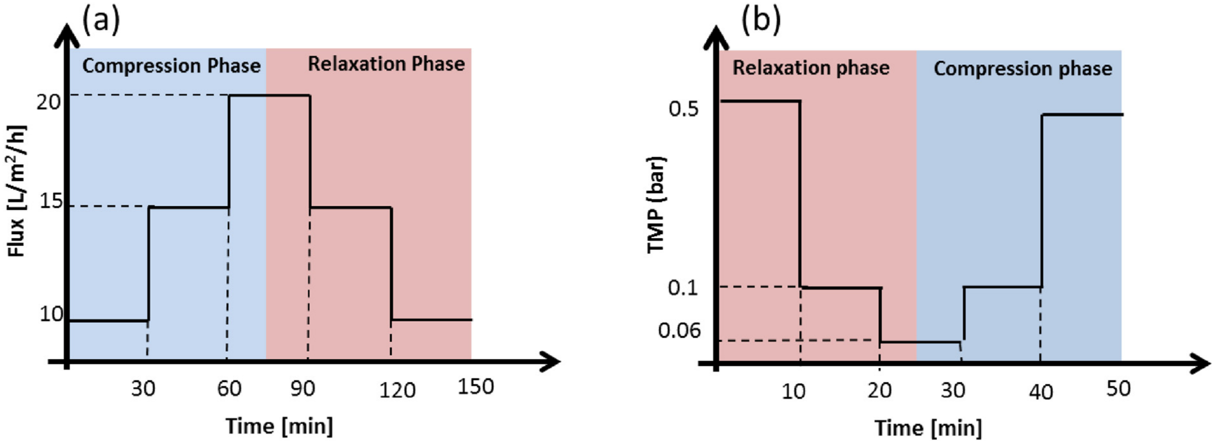

Fig. 1. Schemes of applied loads on the biofilms in this study. a) Step-wise change of permeate flux in time intervals of 30 min for the P-limiting biofilm. b) Step-wise change of transmembrane pressure (TMP) in time intervals of 10 min for the river water biofilm.

biofilm and leads to deformation, while the structural deformation changes the permeability and consequently the pore pressure.

3.1. Model geometry

The biofilms investigated in this study presented mostly a uniform thickness. This implies the main property gradients (e.g., pressure, stress, porosity, permeability) would develop only in the permeate flow direction, i.e., perpendicular to the membrane and biofilm surface (the y direction). A one-dimensional model would therefore be sufficient to describe both water flow and biofilm mechanics. Uniaxial strain for biofilm mechanics would be consistent with the assumption that no deformation (strain) occurs in the lateral directions x and z. However, in order to conveniently use the computational resources already build in COMSOL Multiphysics, we used a two-dimensional model geometry. A rectangular domain was created with the biofilm thickness expanding in the y-direction, taking L_0 as initial thickness. The domain was made very short (5 μm) in the x direction parallel with the membrane. When applying symmetry boundary conditions on the lateral boundaries, this is equivalent with a one-dimensional geometry. Finally, the biofilm depth in the neglected third dimension z was considered large enough to apply the two-dimensional plane-strain simplification. Therefore, we describe here the model equations in the used two-dimensional setup, while the equivalent one-dimensional reduction is presented in the Supplementary Information. The model considered homogeneous biofilm properties in the whole rectangular domain.

3.2. Fluid flow

The biofilm was assumed a porous medium, where Darcy's law, equation (3), and continuity equation (4) were applied to compute fluid (i.e., water) velocity and pressure (Helmig et al., 2013; Pintelon et al., 2012)

$$\mathbf{u} = \frac{-K\varphi}{\mu}\nabla p \tag{3}$$

$$\frac{\partial\varphi}{\partial t} + \nabla\cdot\mathbf{u} = 0 \tag{4}$$

with the local water velocity vector $\mathbf{u}$, pressure p, water viscosity μ, biofilm permeability K and biofilm porosity φ. Biofilm porosity and permeability had to be correlated to the biofilm deformation, in order to represent the effect of structural deformation on the hydraulic resistance and flux. Suppose that the average biofilm porosity scales with biofilm thickness, $\varphi(t)/\varphi_0 = L(t)/L_0$, and that compression mainly affects the pores in the permeation direction (i.e., the quasi-1-D assumption). With these assumptions, the average biofilm porosity at each moment of time can be calculated from eq. (5)

$$\varphi(t) = \varphi_0\frac{L_0 - \int_0^{L(t)} \varepsilon_y(t)dy}{L_0} \tag{5}$$

where φ_0 and L_0 are the initial biofilm porosity and thickness, respectively (i.e., under zero-stress conditions). The total biofilm deformation at a certain time, ΔL, results from integrating the local strain, $\varepsilon_y(t)$, over the whole biofilm thickness L.

Furthermore, the biofilm permeability was calculated from the power-law relation between porosity and permeability as equation (6) proposed by Millington and Quirk (1960):

$$K = A\,\varphi^n \tag{6}$$

with a biofilm permeability coefficient A and permeability exponent n.

In case of the applied step-wise permeate flux, the velocity $\mathbf{u}$=(0, u_y) was imposed on the biofilm base at $y = 0$, where u_y is the applied velocity (permeate flux) taking several values. A constant pressure ($p = p_{top} = 1$ bar) was set on the biofilm-liquid interface. In case of the applied step-wise TMP, the biofilm-liquid interface was subjected to different pressure values to reach the defined TMP. On the biofilm base the flux was set to values calculated from $J = \frac{TMP}{\mu(R_{bio}+R_{mem})}$ as also in (Martin et al., 2014). No-flow conditions were set on the lateral boundaries in all cases.

3.3. Solid mechanics

The reversible response of the biofilm under compression and relaxation experiments implies an elastic behaviour (Korstgens et al., 2001; Paramonova et al., 2009; Stoodley et al., 1999), while the irreversible deformation may be caused by viscous (Galy et al., 2012; Peterson et al., 2015; Safari et al., 2015; Towler et al., 2003) or plastic (Korstgens et al., 2001) components. The time-dependent response to an applied stress is often described by a viscous term. Therefore, based on the experimental observations, we attribute three mechanical behaviours to the biofilm structural response to normal compression and relaxation: elastic, viscoelastic and elastoplastic.

3.3.1. Elastic model

We present here the equations in the general tensor form, while the possible one-dimensional reduction to uniaxial strain is given in Supplementary Information. The biofilm structural mechanics is governed by quasi-static balance of momentum of a linear elastic material, equation (7):

$$\nabla \cdot \boldsymbol{\sigma} = 0 \tag{7}$$

with $\boldsymbol{\sigma}$ the effective stress tensor in the biofilm (Lubliner and Papadopoulos, 2013; Richards, 2000). The constitutive equation (8) relates the stress to elastic forces determined by the stiffness tensor $\mathbf{C}$ (i.e. Hooke's law, here function of elastic modulus E and Poisson's ratio ν), but also to internal forces caused by the fluid pressure p (Coussy, 2004):

$$\boldsymbol{\sigma} = -\alpha\,\mathbf{I}\,p + \mathbf{C}(E,\nu) : \boldsymbol{\varepsilon} \tag{8}$$

In the following it was assumed a Biot-Willis proportionality coefficient $\alpha = 1$. The strain tensor $\boldsymbol{\varepsilon}$ can be expressed from the relative biofilm deformation $\boldsymbol{\delta}$ with respect to the initial biofilm structure, as in equation (9):

$$\boldsymbol{\varepsilon} = \frac{1}{2}\left[(\nabla\boldsymbol{\delta}) + (\nabla\boldsymbol{\delta})^T\right] \tag{9}$$

The values of biofilm mechanical properties (i.e., E and ν) are highly variable as a result of different biofilm composition (i.e., polymers, cells, etc.) and various types of applied stress (i.e., compression/tensile, shear) (Cense et al., 2006; Galy et al., 2012; Klapper et al., 2002; Peterson et al., 2015; Towler et al., 2003). Therefore, these values need to be estimated directly based on the experimental data obtained in this study. The model parameters are presented in Table 1.

In case of the applied step-wise permeate flux, a constant pressure p_{top} was applied on the top boundary, while the biofilm base was fixed (i.e. zero deformation). When a step-wise increase/decrease TMP was applied, the biofilm-liquid interface was subjected to variable pressure p_{top}, while the biofilm base was also fixed. On the lateral boundaries the deformation was considered parallel to the applied stress (i.e., symmetry conditions). These boundary conditions were applied for all three mechanical models (i.e., elastic, elastoplastic and viscoelastic).

3.3.2. Elastoplastic model

The permanent plastic deformation occurs when the biofilm is subjected to a stress higher than a threshold value called “yield stress”. The plastic strain $\boldsymbol{\varepsilon}_p$ must be subtracted from the total strain when used in the constitutive equation (10), leading to:

$$\boldsymbol{\sigma} = -\alpha\,\mathbf{I}\,p \;+\; \mathbf{C}(E,\nu) : (\boldsymbol{\varepsilon} - \boldsymbol{\varepsilon}_p) \tag{10}$$

The constitutive description of plastic behaviour included the yield condition ($F_p = 0$) in which the plastic flow begins when von Mises stress σ_M reaches the initial yield stress σ_{ys0} (Öchsner, 2016):

$$F_p = \sigma_M - \sigma_{ys0} \tag{11}$$

We considered here only the case of ideal plasticity (constant σ_{ys0}, no hardening rule), which described sufficiently well the experimental data. The increment of plastic strain $d\varepsilon_p$ was calculated using the “associated” flow rule eq. (12) (Bland, 1957; Kelly, 2008)

$$d\varepsilon_p = d\lambda \frac{\partial F_p}{\partial \sigma_M} \tag{12}$$

which reduces to $d\varepsilon_p = d\lambda$ for ideal plasticity, with a consistency parameter λ that satisfies the condition $F_p = 0$.

3.3.3. Viscoelastic model

Mechanical behaviour of biological tissues and especially biofilms is often described by a viscoelastic model (Cense et al., 2006; Galy et al., 2012; Klapper et al., 2002; Peterson et al., 2015; Towler et al., 2003). The viscoelastic behaviour is mainly distinguished by a time-dependent deformation under a constant stress. In linear viscoelastic materials the deviatoric stress ($\mathbf{C} : \boldsymbol{\varepsilon}$) depends on strain history. In this study, we used the *Single-branch Generalized Maxwell* model (Peterson et al., 2015) which consists of a spring and dashpot in series (the viscous term), in parallel with the main branch spring (the elastic term). The main branch stiffness is E, while the Maxwell branch is characterized by shear modulus G_v (the spring) and relaxation time τ_v (the dashpot). The total stress is thus augmented by viscoelastic stress $\boldsymbol{\sigma}_v$:

$$\boldsymbol{\sigma} = -\alpha\,\mathbf{I}\,p \;+\; \mathbf{C}(E,\nu) : \boldsymbol{\varepsilon} \;+\; \boldsymbol{\sigma}_v \tag{13}$$

The viscoelastic stress is calculated in terms of strains in spring ε and strain in dashpot γ_v:

Table 1
Model parameters for biofilm compression/relaxation tests under step-wise permeate flux and TMP.

Parameter	Symbol	P-limiting biofilm	River water biofilm	Unit	Source
Biofilm length	l	5	5	μm	Chosen [a]
Initial biofilm thickness	L	980	157	μm	Experimental [b]
Elastic modulus	E	324 ± 7	196	Pa	Fit [b]
Poisson's ratio	ν	0.42	0.42	–	Kundukad et al. (2016)
Initial yield stress	σ_{ys0}	1900	–	Pa	Fit [c]
Viscous shear modulus	G_v	1007.8	–	Pa	Fit [d]
Viscous relaxation time	τ_v	17.4	–	s	Fit [d]
Permeability coefficient	A	~9.9×10^{-16}	1.9×10^{-16}	m^2	Fit [b]
Permeability exponent	n	1.3	1.3	–	(Millington and Quirk, 1960)
Biofilm hardening coefficient	m	0	0.88	–	Fit
Liquid viscosity	μ	0.001	0.001	Pa.s	Water at 25 °C
Biofilm initial porosity	φ_{b0}	0.99	0.99	–	Chosen

[a] Quasi-one-dimensional model assumption.
[b] Values averaged for the three applied models, with standard deviation.
[c] Parameters fitted in the elastoplastic model.
[d] Parameters fitted in the viscoelastic model.

$$\boldsymbol{\sigma}_{\mathrm{v}} = 2G_{\mathrm{v}}(\boldsymbol{\varepsilon} - \boldsymbol{\gamma}_{\mathrm{v}}) \tag{14}$$

with the time-dependent dashpot strain calculated from the differential equation:

$$\tau_{\mathrm{v}}\frac{d\gamma_{\mathrm{v}}}{dt} + \gamma_{\mathrm{v}} = 0 \tag{15}$$

3.4. Model solution

The two-dimensional hydro-mechanical model was solved in COMSOL Multiphysics (v5.2, COMSOL Inc., Burlington, MA). The fluid flow in porous media was coupled with plane strain structural mechanics (Fig. 2). Moving mesh accounted for the biofilm deformation. A time-dependent solver was applied on a mapped finite element mesh (a mesh size of 10 μm ensures the mesh convergence). The parameter fitting was implemented by minimizing the error between experimental and model results, using a MATLAB optimization function through the LiveLink™ for MATLAB.

4. Results and discussion

The biofilm hydraulic resistance depends on biofilm average thickness (depending on local thickness and surface roughness) and permeability. Compression will decrease the biofilm thickness (decreasing resistance), but also decrease the biofilm porosity and permeability (increasing resistance). An increase in biofilm hydraulic resistance decreases in turn the permeate flux.

4.1. Deformation of P-limiting biofilm under controlled permeate flux

The P-limiting biofilm in this study had a smooth surface structure with very low relative roughness, which could be related to the nutrient-limited growth conditions. The river water biofilm selected for this study had also an smooth surface. Table 2 shows the relative biofilm roughness, growth condition and extracellular polymeric substance concentration (EPS) and Fig. 3 presents cross-section images of the studied P-limiting and river water biofilms. The smooth surface biofilm provides a more uniform structural deformation distribution than a biofilm with rough surface. Hence, the homogeneous surface of the biofilms under study provides a valid ground for the plain strain and quasi-one-dimensional model assumptions.

The measured average thickness of the P-limiting biofilm under step-wise flux change over time is presented in Fig. 4. The biofilm thickness changed immediately after each applied step change in flux and remained constant during each time interval of 30 min. During the relaxation phase, the biofilm almost recovers its thickness attained during compression at the same fluxes. This demonstrates the strong elastic component of the biofilm mechanical behaviour. However, a small irreversible biofilm deformation of ~20 μm is visible during flux change from 10 to 15 L/m^2/h (relaxation phase). The permanent biofilm deformation can be explained by a plastic behaviour. An elastoplastic model was therefore applied to explain the experiments. On the other hand, the permanent deformation can also be explained by a viscous behaviour. However, the fact that the thickness reached the stationary value almost immediately after the change in flux indicates that the viscous relaxation time (τ_{v}) is smaller than the data acquisition time (~3 min). Thus, both elastoplastic and viscoelastic models are capable to explain observed results.

The elastic model represents the data reasonably well and it requires the least number of parameters. The determined value of elastic modulus was 317 Pa with the square root of the averaged sum of squares of errors, SRSSE = 13.2 μm. When using the elastoplastic model, a better fit was obtained (SRSSE = 10.6 μm) with $E = 320$ Pa and $\sigma_{ys0} = 1900$ Pa. The viscoelastic model also fitted well the data (SRSSE = 11.3 μm) with $E = 339$ Pa, $G_{\mathrm{v}} = 1008$ Pa and $\tau_{\mathrm{v}} = 17$ s. Therefore, in membrane biofilm studies in which a long-

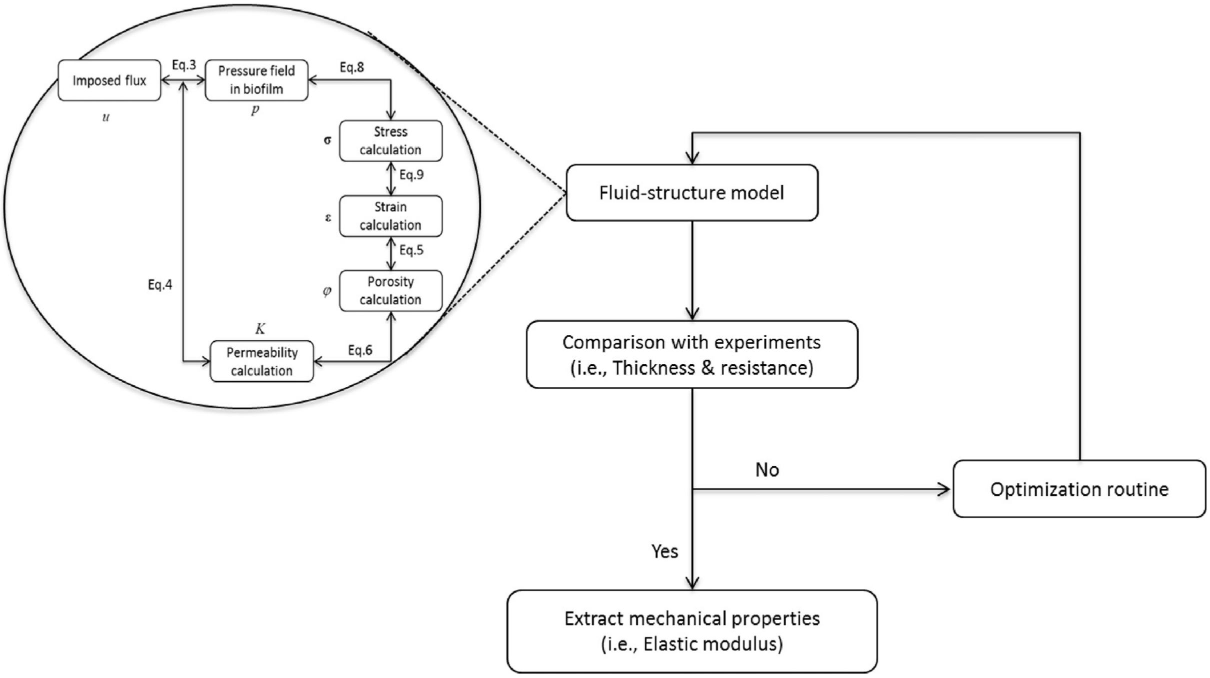

Fig. 2. Flowchart of modelling approach used in this study to extract biofilm mechanical properties. Relation between variables in the fully coupled Fluid-structure model were illustrated in an insert. Reverse arrows indicate that model variables are solved simultaneously (parallel).

Table 2
Growth condition, roughness for the studied biofilms.

Biofilm	Growth condition C/N/P	Relative surface roughness	EPS Concentration (mg C/m^2)[a]
P-limiting biofilm	100/30/0	0.21	676 ± 100
River biofilm	~100/10/10	~0.2	541 ± 15

[a] Based on measurments by Desmond et al. (2018).

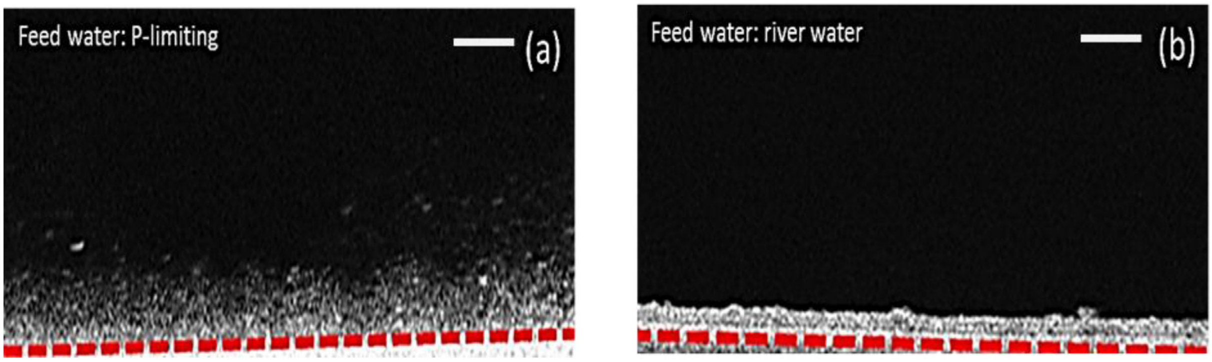

Fig. 3. Two-dimensional cross-section images of (a) P-limiting biofilm (at TMP 0.06 bar) and (b) pre-compressed river water biofilm (at TMP 0.5 bar). Both biofilms show a homogenous surface structure. Dashed-line illustrates the biofilm-membrane interface. Scale bar 200 μm.

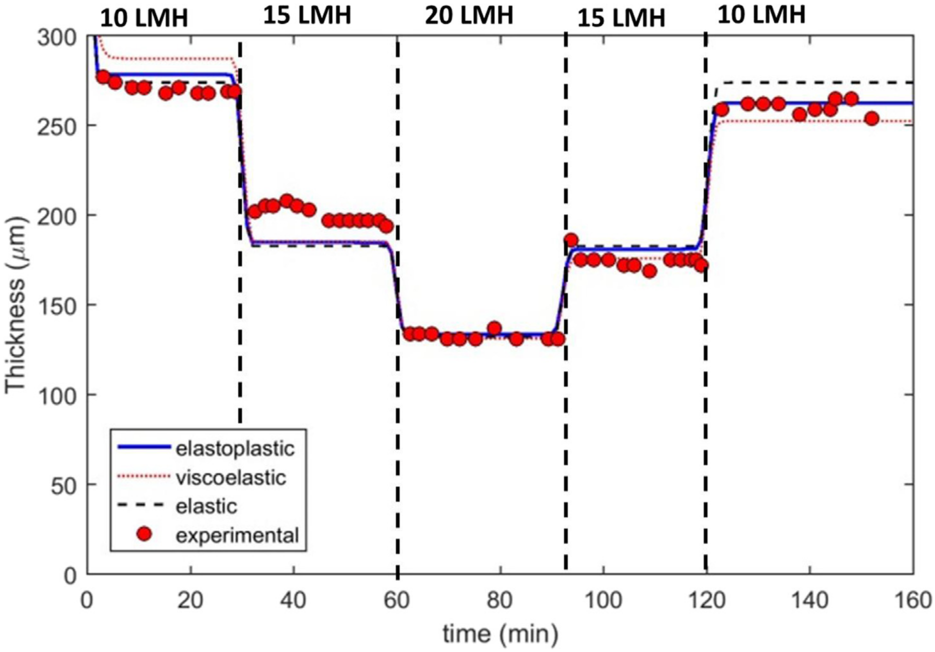

Fig. 4. Experimental (circles) and modelled (lines) thickness of the P-limiting biofilm under step-wise change in permeate flux in a dead-end ultrafiltration (UF) system. The elastic model ($E = 317$ Pa) can explain the reversible deformations, while the elastoplastic ($E = 320$ Pa, $\sigma_{ys0} = 1900$ Pa) and viscoelastic ($E = 339$ Pa, $G_v = 1008$ Pa, $\tau_v = 17$ s) models describe in addition the irreversible deformation observed in the relaxation phase.

term response of biofilm is considered, both viscoelastic and elastoplastic behaviours can equally explain the biofilm response to applied fluxes. However, a simpler elastic model could also describe the observation with only one adjustable parameter instead of two or three.

Fig. 5a demonstrated that thickness reduction of P-limiting biofilm in each identical flux interval is decreased during compression phase (~180, 80 and 60 μm). This behaviour indicates a biofilm stiffening phenomenon ("strength hardening") (Paramonova et al., 2009; Rmaile et al., 2013) during compression. The biofilm compression can be attributed to the permeate drag force, which is induced by the liquid flow (driven by a pore pressure drop across the biofilm). Fig. 5a also shows the initial biofilm thickness $L_0 = 450$ μm under the growth conditions at permeate flux around 5 LMH.

The hydraulic resistance of P-limiting biofilm increases with an increase in permeate flux (Fig. 5b). The biofilm resistance only slightly increased from 1.5×10^{12} to 1.9×10^{12} m^{-1} during the flux increase from 10 to 20 LMH. This relatively minor rise in hydraulic resistance while the biofilm underwent significant structural deformation indicates that the decrease in permeability had a greater effect on hydraulic resistance than the biofilm thickness

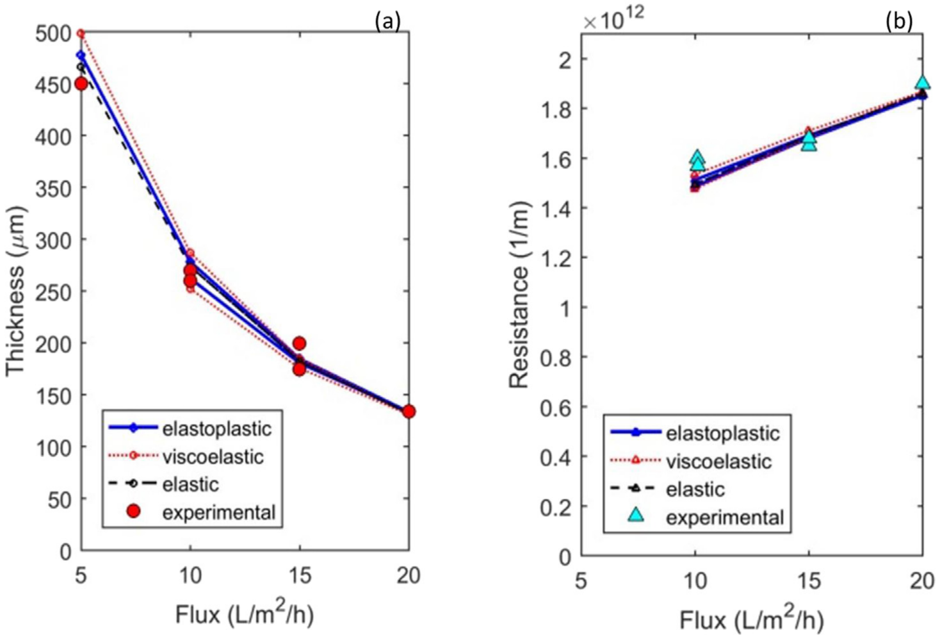

Fig. 5. Structural and hydrological properties of the P-limiting biofilm as a function of permeate flux. a) Time-averaged biofilm thickness during a flux step as a function of flux, experimental and evaluated by three mechanical models; b) Hydraulic resistance of the P-limiting biofilm compared with the model calculations.

reduction. Consequently, all the proposed mechanical models were able to describe the effect of flux on the biofilm resistance (Fig. 5b). The permeability change under compression can be attributed to biofilm structural re-arrangement and void closure, leading to biofilm porosity decrease. Porosity variation was calculated by eq.(5) and permeability function of porosity was computed by eq.(6). The exponent n in eq.(6) tunes the slope of the resistance vs. flux curve, with higher n leading to steeper resistance rise (see Sensitivity Analysis section). The actual porosity change, as calculated, is represented in Fig. 6. The porosity decreased by ~50% in the compression phase while it could be recovered to nearly its initial value in the relaxation phase (Fig. 6).

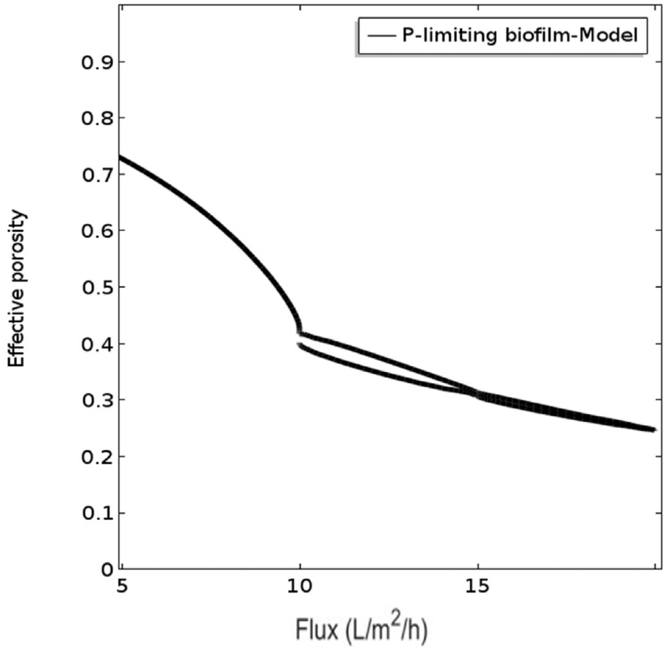

Fig. 6. Computed (elastoplastic model) porosity variation of P-limiting biofilm under step-wise flux changes in a dead-end ultrafiltration system.

4.2. Deformation of river water biofilm under controlled transmembrane pressure

The river water biofilm grown in this study consisted of a mixture of extracellular polymeric substance and cells, as well as particulate matter originating from the influent. The river water biofilm grown in this study included particulate matter originating from the influent, in addition to the typical biofilm composition (mixture of EPS and cells). Biofilms grown under different conditions and influent compositions have different EPS concentration and composition (Desmond et al., 2018). Table 2 shows the measured EPS concentration of both P-limiting and river water biofilms. EPS concentration was higher for the P-limiting biofilm (~676 mg C/m^2) compared to the river biofilm with an EPS concentration of ~541 mg C/m^2. The river water biofilm was grown under 60 mbar TMP in a dead-end UF and it has been subjected to the relaxation/compression scheme presented here (Fig. 1b). A cross-section image of river water biofilm structure is illustrated in Fig. 3b. Similar to the P-limiting biofilm, the river water biofilm expresses a reversible structural response and recoverable deformation during the step-wise unload/load cycle, which can be well described by an elastic model (Fig. 7).

As the applied TMP increased from 0.06 bar to 0.5 bar the biofilm thickness decreases from ~100 to 40 μm (Fig. 8a). The same strain-hardening mechanism in which biofilm stiffness increases as biofilm deforms can be noted here (i.e., less relative deformation as the TMP increases). The fully reversible biofilm deformation measured in this case implies a fully elastic behaviour. However, due to the nonlinear relationship between stress and deformation, the elastic modulus should increase with a decrease in biofilm porosity. Therefore, we proposed an effective Young modulus $E_{eff} = E\,\varphi^{-m}$. The fitted biofilm hardening coefficient m was 0.88 and the $E = 196$ Pa. In this way, the effective Young modulus (i.e., biofilm

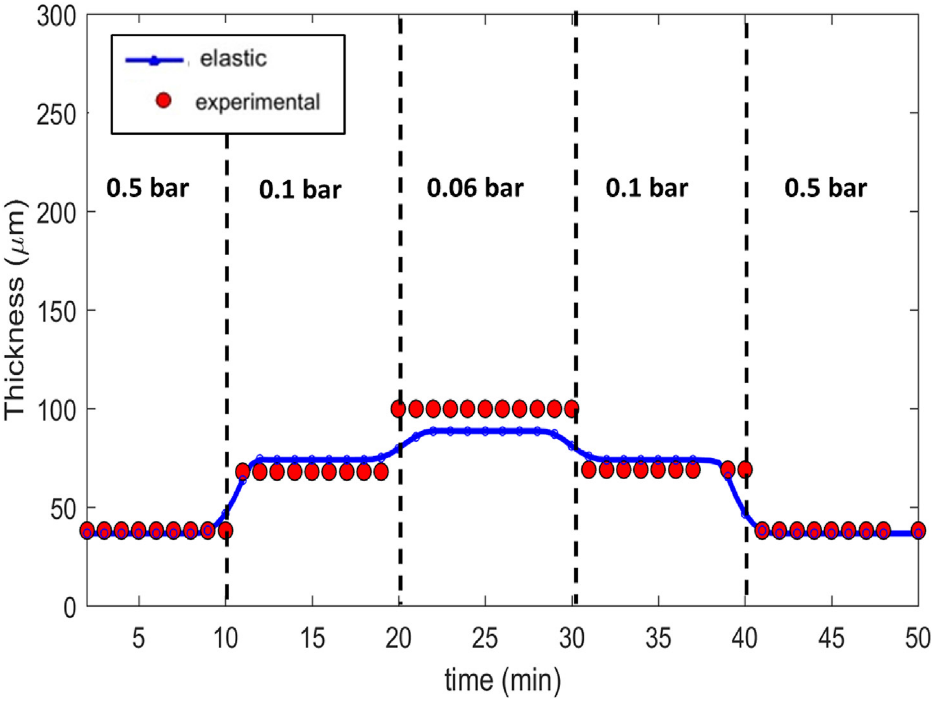

Fig. 7. Thickness of the river water biofilm exposed to step-wise changes in transmembrane pressure (TMP) in a dead-end UF system. The biofilm response to relaxation and compression caused by applied TMP has been evaluated with the elastic model including material stiffening.

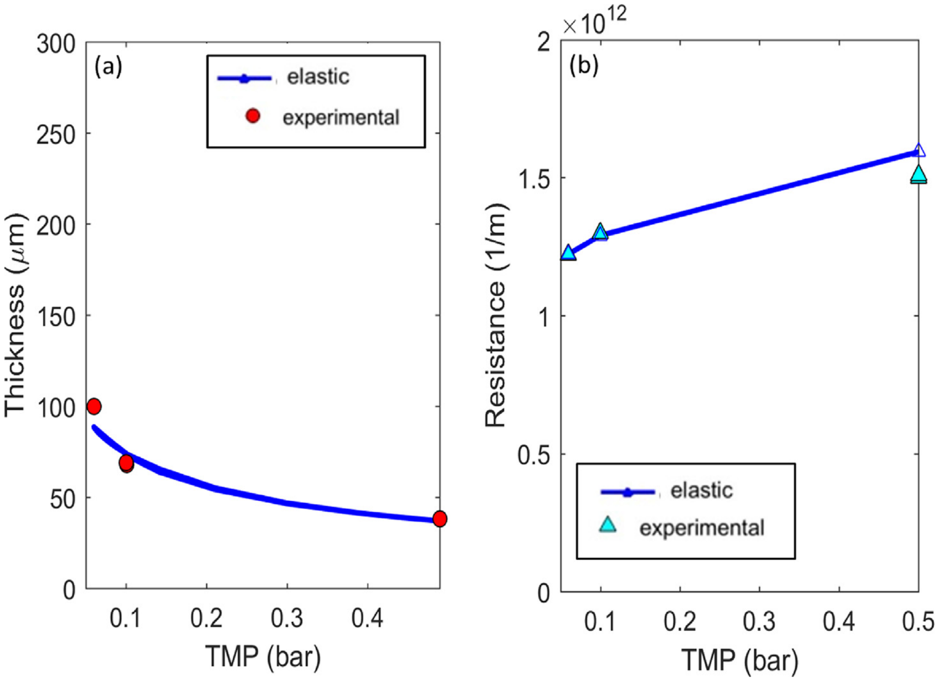

Fig. 8. A comparison between experimental data (symbols) and fluid-structural model results with elastic material behaviour (lines) for the river water biofilm thickness and hydraulic resistance as a function of TMP. a) Time-averaged thickness of the biofilm during TMP steps and model evaluation; b) Hydraulic resistance during TMP steps and model evaluation.

stiffness) increases from ~300 Pa (φ=0.6) to 700 Pa (φ=0.25) when TMP increases from 0.06 to 0.5 bar, respectively (Fig. 9).

Fig. 8b also shows that the river water biofilm hydraulic resistance increases from 1.2×10^{12} to $1.5 \times 10^{12}\ \mathrm{m}^{-1}$ during TMP change from 0.06 to 0.5 bar. Similar to P-limiting biofilm, a decrease in biofilm porosity due to structural deformation causes a slight increase in hydraulic resistance.

Both homogeneous biofilms in this study presented a reversible and recoverable deformation under applied stress (caused either by controlling the flux or the TMP). The deformation in thickness leads to a change hydraulic resistance due to porosity variation.

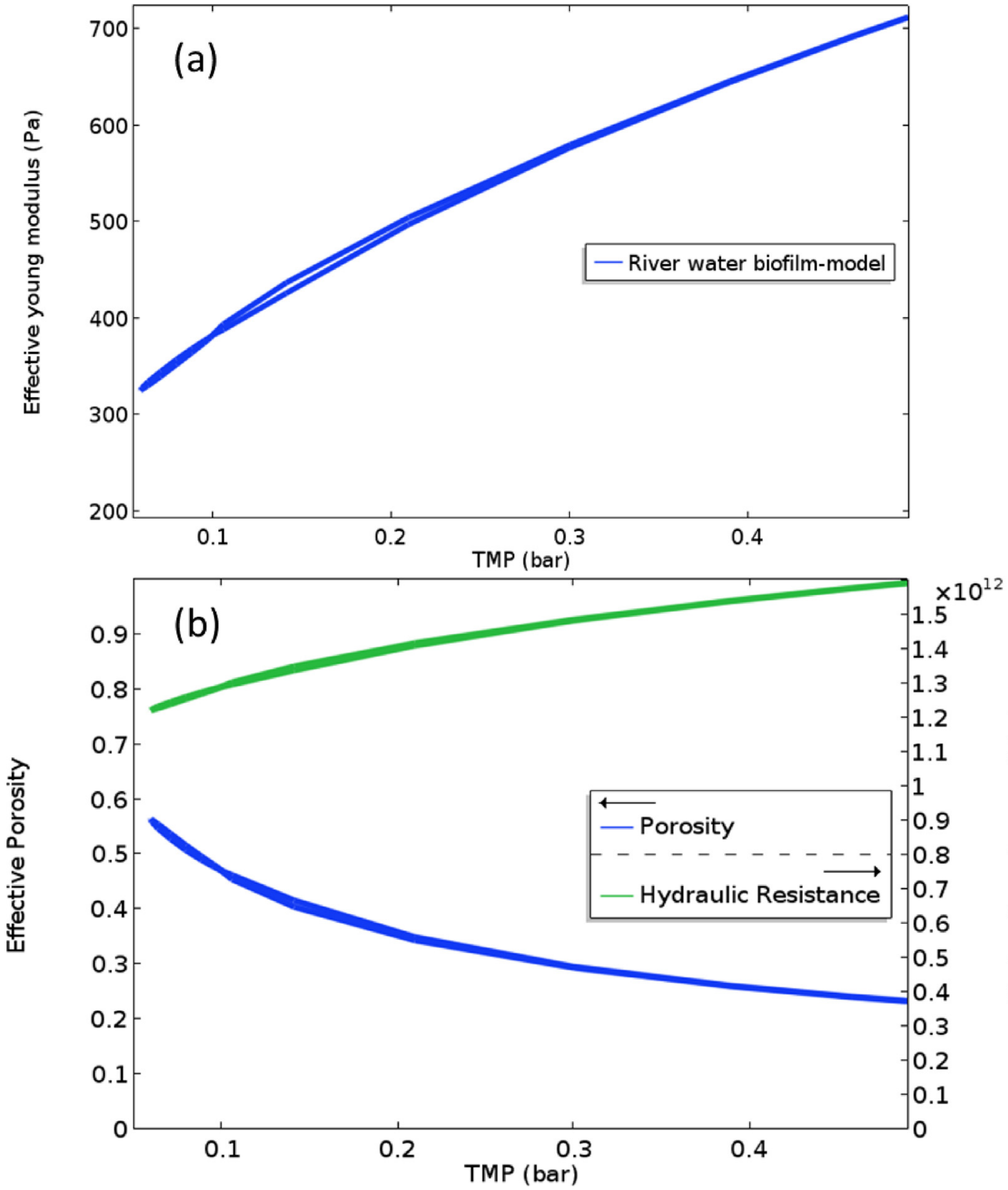

Fig. 9. a) Computed effective elasticity modulus function of applied transmembrane pressure (TMP). River water biofilms showed stain-hardening properties, in which the biofilm stiffness (Young modulus, *E*) increased at elevated TMP. b) Calculated effective porosity and hydraulic resistance of the river biofilm under step-wise TMP. As TMP increases, the biofilm porosity calculated function of biofilm compression would decrease. Pore closure would lead to an increase in biofilm hydraulic resistance.

4.3. *Sensitivity analysis*

Biofilm thickness and hydraulic resistance are the main structural and hydrological properties determined experimentally in this study. To evaluate how mechanical and permeability properties of the biofilm could influence the biofilm thickness and hydraulic resistance, parametric sensitivity simulations were performed with changes in the Young modulus E and hardening coefficient m for the elastic model, shear modulus G_v and relaxation time τ_v for the viscoelastic model, initial yield stress σ_{ys0} for the plastic behaviour, and permeability coefficient A and exponent n for the hydraulic model (Fig. 10).

Mechanical parameters. Biofilms with a higher value of the elastic modulus E have greater stiffness and therefore should undergo smaller structural deformation at a given load (i.e. imposed flux or TMP). Increasing E from 300 to 500 Pa resulted a significant increase in biofilm thickness from ~150 to 250 μm at applied flux of 20 LMH (Fig. 10a).

The biofilm hydraulic resistance only slightly decreased for the similar change in elastic modulus (from 1.45×10^{12} to $1.35 \times 10^{12}\ \mathrm{m}^{-1}$). The effects of biofilm hardening coefficient, m, on biofilm thickness and resistance are shown in Fig. 10d, for a river-water biofilm case. Increasing the biofilm hardening coefficient from 0.4 to 1.2 would result in larger biofilm stiffness during the compression phase and a calculated biofilm thickness reduction from 50 to 100 μm, respectively. However, a change in hardening coefficient had only a minor effect on hydraulic resistance, as shown in Fig. 10d. A variation in the other biofilm mechanical properties (i.e. shear modulus G_v and relaxation time τ_v for the viscoelastic model, or the initial yield stress σ_{ys0} for the plastic

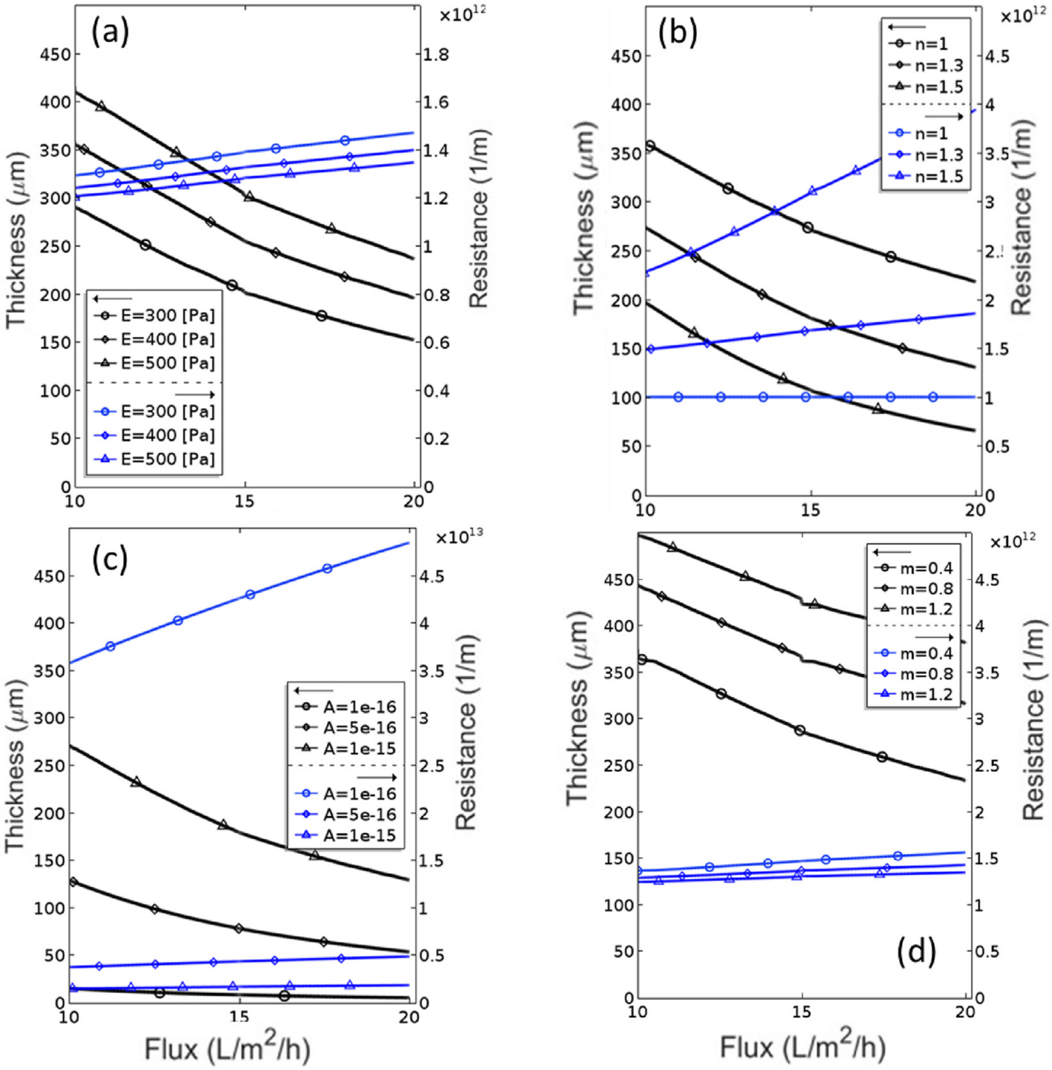

Fig. 10. Parametric study of biofilm thickness and resistance over a flux range for different model parameters: a) elastic modulus, *E*; b) permeability exponent, *n*; c) permeability coefficient, *A*; d) hardening coefficient, *m*. Black lines refer to biofilm thickness variation and blue line show hydraulic resistance. (For interpretation of the references to colour in this figure legend, the reader is referred to the Web version of this article.)

behaviour) in the range often reported for biofilms had only minor influences on the computed biofilm thickness and resistance (Figure S1).

Hydraulic parameters. Biofilm hydraulic parameters (i.e. permeability coefficient A and exponent n in the permeability dependence on the biofilm porosity, eq. (6)) greatly affected biofilm thickness and resistance during step-wise flux change. Increasing the permeability exponent, n, from 1 to 1.5 leads to decrease in the biofilm thickness from ~350 to 200 μm at 10 LMH permeate flux, for the P-limiting biofilm case (Fig. 10b). Practically, the larger the permeability exponent n the steeper the slope of resistance elevation becomes during permeate flux increase. As expected, the change in biofilm permeability coefficient, A, lead to an important thickness and resistance variation (Fig. 10c). For example, increasing permeability coefficient from 1×10^{-16} to 1×10^{-15} m^2 resulted in a biofilm thickness of ~280 to 40 μm at permeate flux equal to10 LMH.

4.4. Discussion

Observed relation between biofilm deformation and hydraulic resistance. It is well experimentally proven that biofilm compression increases the hydraulic resistance and consequently reduces the water permeation through the membrane (Derlon et al., 2016; Desmond et al., 2018; Dreszer et al. 2013, 2014; Valladares Linares et al., 2015). The reversibility in biofilm compression during permeation at changing fluxes or TMPs is related to biofilm composition and morphology (Valladares Linares et al., 2015). *Ex-situ* measurements of biofilm deformation do not provide adequate information on structure dynamics and its effects on biofilm hydraulic resistance, as these only occur in permeation conditions. Thus, applications of microscopy and image processing techniques, particularly OCT but also confocal laser microscopy, for *in-situ* biofilm deformation measurements have attracted attention recently (Blauert et al., 2015; Fortunato et al., 2017). *In-situ* biofilm deformation was measured without permeation under shear forces only (Blauert et al., 2015) or under both permeation and shear force in microfiltration (MF) to evaluate the effect of biofilm compression on the hydraulic resistance (Dreszer et al., 2013). Dreszer et al. (2014) measured biofilm compression and relaxation under step-wise flux change in UF and they observed that biofilm hydraulic resistance significantly increased at elevated permeate fluxes. Later, Valladares Linares et al. (2015) observed biofilm deformation and correlated biofilm thickness under step-wise flux changes in MF to biofilm hydraulic resistance. They observed a clear time-dependent biofilm deformation under permeate flux and interpreted this as a viscoelastic mechanical behaviour. Recently (Desmond et al., 2018), measured biofilm thickness using OCT in dead-end ultrafiltration under a step-wise change in permeate flux and TMP. The biofilm in their study was exposed only to compression forces and the effect of shear force could be neglected due to dead-end conditions in the membrane filtration process.

Biofilm mechanical model. In the present study, we observe reversible compression for both biofilms (Figs. 4 and 7), which could be explained by a simple elastic model. However, for the P-limiting biofilm some small permanent deformation was recorded, which could be interpreted both as viscoelastic and as elastoplastic behaviour. A viscoelastic biofilm is recognized by the time dependency of deformation under constant load (Peterson et al., 2015). However, data from Figs. 4 and 7 demonstrate that the biofilm thickness remained constant under constant applied stress. Still, one should note that in our membrane biofouling study the data acquisition time interval (~minutes) was much larger than the biofilm relaxation time (~seconds) derived from the experiments by (Valladares Linares et al., 2015). Thus, the permanent biofilm deformation could still be described by a viscoelastic model, while remaining in agreement with a plastic characteristic too. All these lead to the conclusion that the observed mechanical behaviour of the biofilm not only depends on biofilm composition and morphology, but also on the type of applied stress (e.g., shear by flow over the biofilm, compression by permeation flow, etc.) and on the time-scale of observations.

Biofilm hydraulics. Hydraulic resistance of biofilms depends on the biofilm structure (e.g., thickness, surface roughness and porosity) and permeability characteristics. Figs. 5b and 8b demonstrate that biofilm compression is accompanied by a small increase in biofilm hydraulic resistance under elevated flux or TMP. Assuming that the biofilm permeability does not vary due to compression, the biofilm hydraulic resistance should decrease as a result of its thickness reduction. The slight increase in hydraulic resistance clearly indicates that the effect of permeability reduction due to pore closure determines biofilm hydraulic resistance instead of biofilm shrinkage (i.e., shortening the permeation distance). The proposed models thus imply that the biofilm compression mainly occurs by pore shrinkage and that the pores are partially restored during the relaxation phase. Dreszer et al. (2013) and Valladares Linares et al. (2015) reported much stronger increase in hydraulic resistance under elevated fluxes than results of this study presented. Such deviation could be explained by the differences in biofilm morphology among these investigations. Heterogeneous biofilms (i.e., fluffy, filamentous, “mushroom-like”, etc.) in these studies would collapse under applied stress, leading to macro-pore closure or channel blocking, ultimately resulting in a significant rise of hydraulic resistance. Moreover, biofilm structure collapse would lead to irreversible biofilm compression. Since the biofilms in our study had only a low surface roughness, demonstrating reversible and recoverable deformation under compression, accompanied by a slight increase observed in the hydraulic resistance. Therefore, for a biofilm with homogeneous surface (i.e., planar, flat, smooth, etc.), the compression could mainly affect the structural deformation, not the hydrological properties (i.e. hydraulic resistance).

Biofilm porosity. The calculated porosity changed significantly during the compression and relaxation cycles (mostly between 0.75 and 0.25, Figs. 6 and 9b). In order to better estimate the model parameters (mechanical and hydraulic), the biofilm porosity would have to be determined independently during the permeation experiments. Measurements of biofilm porosity were reported by Blauert et al. (2015), who estimated a change in 5–10% porosity during their shear flow tests – but such measurements would also be needed under permeation conditions. However, it should be noted that biofilm porosity measurement is really challenging for multiple reasons. First, the biofilm fragile structure can be damaged in *ex-situ* techniques. Second, the pore distinction in *in-situ* techniques using image processing can be ambiguous (i.e., grey-scale thresholding, non-repetitive image brightness/contrast, interpretation of grey-scale image, pore distinction criteria, etc.). Finally, the porosity observed by visual/microscopic/imaging techniques - i.e., apparent voids in the biofilm structure - may not be directly correlated with the hydraulic porosity. Thus, back-calculation of biofilm porosity using structural and hydrological properties (i.e., thickness and hydraulic resistance) might lead to more reliable porosity values.

Biofilm structural hardening. Biofilm thickness during compression/relaxation phases depends on biofilm composition (i.e., cells, polymers, mineral inclusions, all with different mechanical properties), biofilm morphology (i.e., surface roughness and porosity) and applied load magnitude and direction (i.e., shear or normal forces). Several studies show how biofilm mechanical properties depend on biofilm composition and morphology (Dreszer et al., 2013; Peterson et al., 2015; Stoodley et al., 1999). Laspidou et al. (2014) demonstrates with a numerical model that the biofilm mechanical properties change during compression and tension tests. They also showed that biofilm mechanical properties can vary with the biofilm structure. All these observations and theories support the definition of effective mechanical properties which integrate biofilm material properties (intrinsic Young modulus, but probably also viscoelastic or elastoplastic parameters) with biofilm hydrological and structural properties (i.e. porosity).

The step-wise flux change experiments showed that biofilm stiffness increases at greater permeation fluxes, leading to smaller thickness reduction during compression. Biofilms in this study showed a strain hardening behaviour that can be represented quantitatively by the hardening coefficient, m. Biofilm with higher values of hardening coefficient become stiffer under applied load (Fig. 9a) and consequently smaller deformation occurs under elevated fluxes (Fig. 10d). The strain-hardening behaviour of biofilms was already reported by (Paramonova et al., 2009) for dental biofilms, similarly described before for rubber-like materials. This tendency could be explained by the fact that at mild compression forces the biofilm pores take up the stress and gradually close, while at higher loads the polymers and cells (harder biofilm constituents) would oppose the applied load. In this respect, Valladares Linares et al. (2015) demonstrated that EPS concentration in the biofilm is a dominant factor in determining mechanical properties and biofilm thickness variation. We proposed here a simple power-law correlation of the elasticity modulus with the porosity, $E_{eff} = E\,\varphi^{-m}$. However, in the literature there are several other alternatives, such as, the Ryshkewitch-Duckworth equation (Ryshkewitch, 1953) proposed for porous sintered materials, $E_{eff} = E\exp(-m\,\varphi)$, or the Phani-Niyogi equation (Phani and Niyogi, 1987) using another power-law formulation $E_{eff} = E\,(1 - \varphi/\varphi_{crit})^m$ which implies the existence of a critical porosity at which the Young modulus becomes zero (Blauert, 2017).

Mechanical properties. Values of Young (elastic) modulus reported in literature vary in a wide range between ~10 and 6000 Pa (Korstgens et al., 2001; Mohle et al., 2007; Peterson et al., 2015; Stoodley et al., 1999) based on biofilm type and applied mechanical tests. For example, Stoodley et al. (1999) reported elastic moduli between 17 and 240 Pa for biofilms exposed to different shear levels, while (Paramonova et al., 2009) reported similar values of ~20–200 Pa for dental biofilms also under variable shear. Blauert et al. (2015) reported a shear modulus of around 30 Pa for biofilm under shear stress using OCT and deformation angles, which corresponds to $E = 80$ Pa when Poisson ratio is 0.4. However, under uniaxial compression, much higher values were reported, $E \approx 6500$ Pa (Korstgens et al., 2001). In this study we found elastic moduli E of ~320 Pa for P-limiting biofilm and ~200 Pa for river water biofilm, well in the range reported in literature. The variation of measured Young modulus can be attributed to different biofilm composition, different mechanical tests (compression, tensile, shear) and also different measurements techniques (rheometer, image processing, etc.). One should note that mechanical properties in this work were calculated for biofilms under compression forces, for which Aravas and Laspidou (2008) demonstrated that larger values should be obtained compared to shear tests. Moreover, viscoelastic properties fitting data from this study were shear modulus $G_v \approx 1000$ Pa and biofilm relaxation time $\tau_v \approx 17$ s. The biofilm relaxation times often reported in literature are in the order magnitude of seconds, in-line with the value reported here (Towler et al., 2003; Valladares Linares et al., 2015). Moreover, biofilm shear modulus ($G_v \approx 1000$ Pa) is well in the range of the value reported for Maxwell shear modulus for two type of biofilm by Jones et al. (2011).

Permeability properties. Although, biofilm structure response to applied forces is greatly influenced by the elastic modulus, its impact on hydraulic resistance did not appear considerable in our study. This again can be explained by the fact that, in homogeneous biofilms, the hydraulic resistance is mainly governed by porosity change by pore closure and not by thickness decrease. On the other hand, sensitivity analysis simulations showed that the biofilm permeability coefficient, A, and permeability exponent, n, determine the biofilm hydraulic resistance (Fig. 10b and c). Increasing values of A and n would result in higher permeability and therefore higher stress exerted on the biofilm leading to a considerable structural deformation, as well as permeability change. The correlation proposed here between biofilm permeability and porosity can be applied for biofilms with high surface roughness but with a higher value of exponent coefficient, n.

Future research. To increase accuracy of experimental results and model validation more number of TMP steps need to be evaluated. In the current study, TMP steps selection were facing three main problems: 1) make sure that compression would occur in the smaller range of TMP; 2) lower TMP steps would result a very small change in the collected permeate mass (used in the calculation of biofilm resistance) and, consequently, the changes in hydraulic resistances for different TMP steps would be negligible and results would become doubtable; 3) another issue for smaller TMP steps was that reaching a stable TMP value in a small step was difficult with the existing PID control system. Therefore, the proposed approach in the study of biofilm compressibility should be evaluated for a wider TMP range and more TMP steps.

Knowledge of biofilm mechanics is essential to optimize physical cleaning strategies such as shear cleaning (Hilal et al., 2005), air bubble cleaning (Wibisono et al., 2014), air/water jet cleaning (Fabbri et al., 2016; Safari et al., 2015). Non-invasive methodologies to obtain biofilm mechanical properties should be developed. For this aim, OCT data coupled with a fluid-structure numerical model can provide an opportunity to estimate biofilm mechanical properties in a non-destructive way. The present work focused on uniaxial biofilm compression driven by flow. A fully coupled fluid-structural model for heterogeneous surface biofilm also needs to be developed, in order to use the two- or three-dimensional datasets obtainable by OCT. In this way, the spatial variation of mechanical properties within heterogeneous biofilms could be estimated. For such a goal, experimental determination of local deformations in the biofilm is needed (for example, by using embedded particles (Galy et al., 2012) or other particle tracking methods). Development of more complex material models to simulate deformation non-linearity may be required. Coupling biofilm mechanics with flow, would also need the development of reliable experimental techniques to measure biofilm hydraulic porosity.

5. Conclusions

- A poroelastic computational model which couples water permeation through the biofilm with the biofilm mechanics was developed to correlate the structural deformation with biofilm hydraulic resistance.
- Mechanical and hydraulic biofilm properties were estimated based on the data obtained in compression/relaxation cycles, with a fully coupled fluid-structural model.
- The hydraulic resistance of the smooth surface biofilms (e.g., grown in P-limiting conditions) under compression was affected more by permeability decrease due to pore closure than by a decrease in thickness.
- In membrane biofilm compression studies with sampling time step larger than the biofilm relaxation time, both viscoelastic and elastoplastic models could describe the permanent biofilm deformation. For biofilms under study, due to the small irreversible deformation, a simpler elastic model could also be used.
- The elastic moduli fitting the measured data were in agreement with other reported values for biofilm under compression. Biofilm stiffening under larger flow-driven compression forces was observed and described numerically by correlating inversely the elastic modulus with biofilm porosity.

Acknowledgements

This study was funded by European Union's Horizon 2020 research and innovation programme under the Marie Skłodowska-Curie grant agreement No. 676070 and the Swiss National Science Foundation BIOMEMBRA project, grant No. 149648. This communication reflects only the authors' view and the Research Executive Agency of the EU is not responsible for any use that may be made of the information it contains.

Appendix A. Supplementary data

Supplementary data related to this article can be found at https://doi.org/10.1016/j.watres.2018.08.036.

References

Aravas, N., Laspidou, C.S., 2008. On the calculation of the elastic modulus of a biofilm streamer. Biotechnol. Bioeng. 101 (1), 196–200.

Bland, D.R., 1957. The associated flow rule of plasticity. J. Mech. Phys. Solid. 6 (1), 71–78.

Blauert, F., 2017. Investigating Biofilm Deformation Using Optical Coherence Tomography and Fuid-structure Interaction Simulation. Karlsruher Instituts fur Technologie, Karlsruhe.

Blauert, F., Horn, H., Wagner, M., 2015. Time-resolved biofilm deformation measurements using optical coherence tomography. Biotechnol. Bioeng. 112 (9), 1893–1905.

Casey, E., 2007. Tracer measurements reveal experimental evidence of biofilm consolidation. Biotechnol. Bioeng. 98 (4), 913–918.

Cense, A.W., Peeters, E.A.G., Gottenbos, B., Baaijens, F.P.T., Nuijs, A.M., van Dongen, M.E.H., 2006. Mechanical properties and failure of Streptococcus mutans biofilms, studied using a microindentation device. J. Microbiol. Meth. 67 (3), 463–472.

Coussy, O., 2004. Poromechanics. Wiley, UK.

Derlon, N., Grutter, A., Brandenberger, F., Sutter, A., Kuhlicke, U., Neu, T.R., Morgenroth, E., 2016. The composition and compression of biofilms developed on ultrafiltration membranes determine hydraulic biofilm resistance. Water Res. 102, 63–72.

Desmond, P., Morgenroth, E., Derlon, N., 2018. Physical structure determines compression of membrane biofilms during Gravity Driven Membrane (GDM) ultrafiltration. Water Res. 143, 539–549.

Dreszer, C., Vrouwenvelder, J.S., Paulitsch-Fuchs, A.H., Zwijnenburg, A., Kruithof, J.C., Flemming, H.C., 2013. Hydraulic resistance of biofilms. J. Membr. Sci. 429, 436–447.

Dreszer, C., Wexler, A.D., Drusova, S., Overdijk, T., Zwijnenburg, A., Flemming, H.C., Kruithof, J.C., Vrouwenvelder, J.S., 2014. In-situ biofilm characterization in membrane systems using Optical Coherence Tomography: formation, structure, detachment and impact of flux change. Water Res. 67, 243–254.

Fabbri, S., Johnston, D.A., Rmaile, A., Gottenbos, B., De Jager, M., Aspiras, M., Starke, E.M., Ward, M.T., Stoodley, P., 2016. Streptococcus mutans biofilm transient viscoelastic fluid behaviour during high-velocity microsprays. J Mech Behav Biomed Mater 59, 197–206.

Fortunato, L., Qamar, A., Wang, Y., Jeong, S., Leiknes, T., 2017. In-situ assessment of biofilm formation in submerged membrane system using optical coherence tomography and computational fluid dynamics. J. Membr. Sci. 521, 84–94.

Galy, O., Latour-Lambert, P., Zrelli, K., Ghigo, J.M., Beloin, C., Henry, N., 2012. Mapping of bacterial biofilm local mechanics by magnetic microparticle actuation. Biophys. J. 103 (6), 1400–1408.

Helmig, R., Flemisch, B., Wolff, M., Ebigbo, A., Class, H., 2013. Model coupling for multiphase flow in porous media. Adv. Water Resour. 51, 52–66.

Herzberg, M., Elimelech, M., 2007. Biofouling of reverse osmosis membranes: role of biofilm-enhanced osmotic pressure. J. Membr. Sci. 295 (1), 11–20.

Hilal, N., Ogunbiyi, O.O., Miles, N.J., Nigmatullin, R., 2005. Methods employed for control of fouling in MF and UF membranes: a comprehensive review. Separ. Sci. Technol. 40 (10), 1957–2005.

Jones, W.L., Sutton, M.P., McKittrick, L., Stewart, P.S., 2011. Chemical and antimicrobial treatments change the viscoelastic properties of bacterial biofilms. Biofouling 27 (2), 207–215.

Kelly, P., 2008. Mechanics lecture notes: an introduction to solid mechanics. http://homepages.engineering.auckland.ac.nz/~pkel015/SolidMechanicsBooks/.

Klapper, I., Rupp, C.J., Cargo, R., Purvedorj, B., Stoodley, P., 2002. Viscoelastic fluid description of bacterial biofilm material properties. Biotechnol. Bioeng. 80 (3), 289–296.

Korstgens, Flemming, H.-C., Wingender, J., Borchard, W., 2001. Uniaxial compression measurement device for investigation of the mechanical stability of biofilms. J. Microbiol. Meth. 46, 9–17.

Kundukad, B., Seviour, T., Liang, Y., Rice, S.A., Kjelleberg, S., Doyle, P.S., 2016. Mechanical properties of the superficial biofilm layer determine the architecture of biofilms. Soft Matter 12 (26), 5718–5726.

Laspidou, C.S., 2007. Variation in the mechanical properties of a porous multi-phase biofilm under compression due to void closure. Water Sci. Technol. 55 (8–9), 447.

Laspidou, C.S., Spyrou, L.A., Aravas, N., Rittmann, B.E., 2014. Material modeling of biofilm mechanical properties. Math. Biosci. 251, 11–15.

Lee, S., Boo, C., Elimelech, M., Hong, S., 2010. Comparison of fouling behavior in forward osmosis (FO) and reverse osmosis (RO). J. Membr. Sci. 365 (1), 34–39.

Li, Q., Elimelech, M., 2004. Organic fouling and chemical cleaning of nanofiltration Membranes: measurements and mechanisms. Environ. Sci. Technol. 38 (17), 4683–4693.

Lubliner, J., Papadopoulos, P., 2013. Introduction to Solid Mechanics: an Integrated Approach. Springer, New York.

Martin, K.J., Bolster, D., Derlon, N., Morgenroth, E., Nerenberg, R., 2014. Effect of fouling layer spatial distribution on permeate flux: a theoretical and experimental study. J. Membr. Sci. 471, 130–137.

Millington, R., Quirk, P., 1960. Permeability of porous solids. Trans. Faraday Soc. 57, 1200–1207.

Mohle, R.B., Langemann, T., Haesner, M., Augustin, W., Scholl, S., Neu, T.R., Hempel, D.C., Horn, H., 2007. Structure and shear strength of microbial biofilms as determined with confocal laser scanning microscopy and fluid dynamic gauging using a novel rotating disc biofilm reactor. Biotechnol. Bioeng. 98 (4), 747–755.

Öchsner, A., 2016. Elasto-plasticity of Frame Structure Elements: Modeling and Simulation of Rods and Beams. Springer, Berlin, Heidelberg.

Paramonova, E., Kalmykowa, O.J., van der Mei, H.C., Busscher, H.J., Sharma, P.K., 2009. Impact of hydrodynamics on oral biofilm strength. J. Dent. Res. 88 (10), 922–926.

Peterson, B.W., He, Y., Ren, Y., Zerdoum, A., Libera, M.R., Sharma, P.K., van Winkelhoff, A.J., Neut, D., Stoodley, P., van der Mei, H.C., Busscher, H.J., 2015. Viscoelasticity of biofilms and their recalcitrance to mechanical and chemical challenges. FEMS Microbiol. Rev. 39 (2), 234–245.

Phani, K.K., Niyogi, S.K., 1987. Young's modulus of porous brittle solids. J. Mater. Sci. 22 (1), 257–263.

Pintelon, T.R.R., Picioreanu, C., Loosdrecht, M.C.M.v., Johns, M.L., 2012. The effect of biofilm permeability on bio-clogging of porous media. Biotechnol. Bioeng. 109 (4), 1031–1042.

Radu, A.I., Vrouwenvelder, J.S., van Loosdrecht, M.C.M., Picioreanu, C., 2010. Modeling the effect of biofilm formation on reverse osmosis performance: flux, feed channel pressure drop and solute passage. J. Membr. Sci. 365 (1), 1–15.

Richards, R., 2000. Principles of Solid Mechanics. CRC Press, Florida, US.

Rmaile, A., Carugo, D., Capretto, L., Zhang, X., Wharton, J.A., Thurner, P.J., Aspiras, M., Ward, M., Stoodley, P., 2013. Microbial tribology and disruption of dental plaque bacterial biofilms. Wear 306 (1–2), 276–284.

Ryshkewitch, E., 1953. Compression strength of porous sintered alumina and zirconia. J. Am. Ceram. Soc. 36 (2), 65–68.

Safari, A., Tukovic, Z., Walter, M., Casey, E., Ivankovic, A., 2015. Mechanical properties of a mature biofilm from a wastewater system: from microscale to macroscale level. Biofouling 31 (8), 651–664.

Stoodley, P., Lewandowski, Zbigniew, Boyle, John D., Lappin-Scott, H.M., 1999. Structural deformation of bacterial biofilms caused by short-term fluctuations in fluid shear: an in situ investigation of biofilm rheology. Biotechnol. Bioeng. 65 (1).

Towler, B.W., Rupp, C.J., Cunningham, A.B., Stoodley, P., 2003. Viscoelastic properties of a mixed culture biofilm from rheometer creep analysis. Biofouling 19 (5), 279–285.

Valladares Linares, R., Wexler, A.D., Bucs, S.S., Dreszer, C., Zwijnenburg, A., Flemming, H.C., Kruithof, J.C., Vrouwenvelder, J.S., 2015. Compaction and relaxation of biofilms. Desalination and Water Treatment 57 (28), 12902–12914.

Vrouwenvelder, H.S., van Paassen, J.A.M., Folmer, H.C., Hofman, J.A.M.H., Nederlof, M.M., van der Kooij, D., 1998. Biofouling of membranes for drinking water production. Desalination 118 (1), 157–166.

Vrouwenvelder, J.S., Hinrichs, C., Van der Meer, W.G.J., Van Loosdrecht, M.C.M., Kruithof, J.C., 2009. Pressure drop increase by biofilm accumulation in spiral wound RO and NF membrane systems: role of substrate concentration, flow velocity, substrate load and flow direction. Biofouling 25 (6), 543–555.

Wibisono, Y., Cornelissen, E.R., Kemperman, A.J.B., van der Meer, W.G.J., Nijmeijer, K., 2014. Two-phase flow in membrane processes: a technology with a future. J. Membr. Sci. 453, 566–602.

Xie, M., Lee, J., Nghiem, L.D., Elimelech, M., 2015. Role of pressure in organic fouling in forward osmosis and reverse osmosis. J. Membr. Sci. 493, 748–754.